

¹ Department of Atmospheric Sciences and Global Environment Laboratory, Yonsei University, Seoul, Korea

² Department of Environmental Science and Engineering, Kwangju Institute of Science and Technology, Kwangju, Korea

Some Aspects of Internal Gravity Waves in the Multicell-Type Convective System

H.-Y. Chun¹, I.-S. Song¹, and J.-J. Baik²

With 14 Figures

Received March 4, 1998

Revised July 20, 1998

Summary

Some aspects of internal gravity waves in the multicell-type convective system are examined using a linear theory and a nonlinear numerical model. The basic-state wind is assumed to increase linearly with height and then remain constant.

In the theoretical part, the two-dimensional, linear, steady-state response of a stably stratified atmosphere to specified cooling representing the evaporative cooling of falling precipitation in the subcloud layer is analytically considered. It is shown that there exist an updraft on the upstream side of the cooling and a downdraft on the downstream side. As the wind shear increases enough, the magnitude of the updraft decreases. This is because a large portion of the specified cooling is used to compensate for the positive vorticity associated with the positive wind shear and accordingly the effective cooling necessary to produce perturbations is reduced.

In the numerical part, a two-dimensional version of the ARPS (Advanced Regional Prediction System) that is a nonhydrostatic, compressible model with detailed physical processes is employed. Results from the dry simulation, in which the steady cooling is specified in the model, show that the simulated quasi-steady field resembles the linear, steady-state solution field because the nonlinearity factor of thermally-induced waves in this case is small. For the moist simulation, the quasi-steady perturbations obtained from the dry simulation are used as initial conditions. It is shown that gravity waves can effectively initiate convection even with small amplitude and that updraft at the head of the density current somewhat resembles the linear, steady-state response of a stably stratified flow to the specified cooling. The updraft, that is, forced internal gravity waves, at the head of the density current is responsible for the initiation

of consecutive convective cells that move downstream and develop as a main convective cell. This study suggests that internal gravity waves play a major role in the initiation of consecutive convective cells in the multicell-type convective system and hence in its maintenance.

1. Introduction

The mechanisms of initiation, development, and maintenance of mesoscale convective system producing severe weather such as localized heavy precipitation, thunderstorms, gust winds, etc. have been extensively studied during the past two decades. This kind of mesoscale convective system lasts longer than six hours sometimes, while the life cycle of a single convective cell is usually less than an hour. Therefore, research has focused on understanding the maintenance mechanism of the convective system.

It has been known based on numerical modeling studies (e.g., Weisman and Klemp, 1982; Rotunno et al., 1988) that mesoscale convective system, at least the line-type convection such as squall lines, can be sustained by the vorticity balance between the cold pool induced by the evaporative cooling of falling precipitation and the basic-state wind shear. The cold outflow propagating upstream and relatively warm and humid inflow produce a convective updraft cell at the leading edge of the outflow, named the gust

front. The cell develops and produces precipitation. Therefore, mesoscale convective system can be maintained by producing consecutive new cells in the system. Updraft at the gust front can be considered to be forced internal gravity waves induced by the cold pool generated by the evaporative cooling of falling precipitation. These internal gravity waves representing the updraft at the gust front are one of important factors in maintaining the convective system.

In the numerical studies of multicell storms, the mechanisms of convective cell generation, development, and propagation have been main research topics. Fovell and Ogura (1988) simulated the quasi-steady state of multicell storm with a regular period of cell generation at the head of the gust front. It was shown that consecutive cells propagate rearward by the front-to-rear inflow. In a following study, Fovell and Ogura (1989) investigated the effects of environmental wind shear on multicell storms. They showed that the density current speed is linearly proportional to the magnitude of wind shear specified in the lowest 2.5 km. The effects of shear layer depth on the regularity of cell regeneration were examined by Fovell and Dailey (1995). The importance of internal gravity waves in multicell-type storms has been brought out by Yang and Houze (1995). They suggested that the consecutive cells behind the updraft at the gust front are propagating gravity waves trapped in the convective region based on the phase relationship of the simulated flow fields. Pandya and Durran (1996) suggested that overall mesoscale circulation around squall lines is gravity waves induced by the latent heating and cooling. They mentioned that the nonlinear dynamics of squall lines results in the consecutive cells behind the leading updraft. Lin et al. (1998) proposed an advection mechanism to explain the cell regeneration of multicell storms, which is different from Yang and Houze's (1995) gravity wave processes. They showed that there are two stages of rearward propagating consecutive cells behind the gust front updraft. One is the growing stage that should experience a critical level in order to have an amplification and the other is the propagating stage that has the characteristics of gravity waves. Using the phase relationship between vertical velocity and latent heating, they proposed that the consecutive cells

are forced gravity waves induced by diabatic heating rather than trapped gravity waves suggested by Yang and Houze (1995).

In theoretical studies (Lin and Smith, 1986; Lin and Chun, 1991; Chun and Lin, 1995), updraft at the gust front is considered to be internal gravity waves induced by steady cooling in a stably stratified flow. Lin and Chun (1991) showed that the magnitude and structure of the updraft are determined by the relative magnitudes between the density current speed and the inflow wind speed. Lin et al. (1993) investigated interactions between gravity waves and cold outflows in a stably stratified uniform flow. The maintenance of multicell storm is strongly dependent upon its ability to lift warm and humid inflow air to the level of free convection. That is, it depends on the magnitude and structure of gravity waves.

In this study, we examine some aspects of internal gravity waves in the multicell-type convective system using both a linear theory and a nonlinear numerical model. In the theoretical part, the two-dimensional, linear, steady-state response of a stably stratified atmosphere to specified cooling is investigated. The cooling represents the evaporative cooling of falling precipitation in the subcloud layer of the convective system. In the numerical part, two model simulations are conducted – a dry simulation with specified cooling representing the evaporative cooling of falling precipitation and a moist simulation that includes explicit cloud microphysical processes. In the dry simulation, the linear, steady-state perturbations obtained in the theoretical part are used as initial conditions. In the moist simulation, the quasi-steady perturbations obtained from the dry simulation are used as initial conditions and convection is initiated by the quasi-steady perturbations. This approach gives model-consistent gravity waves.

2. Theoretical Consideration

2.1 Governing Equations and Solutions

Updraft at the gust front, which is an important factor in maintaining mesoscale convective system, can be regarded as the forced gravity-wave response of a stably stratified flow to

diabatic cooling. In this section, we consider two-dimensional, linear, steady-state perturbations in a hydrostatic, Boussinesq, inviscid, nonrotating flow system. The equations governing small-amplitude perturbations can be written as

$$U \frac{\partial u}{\partial x} + \frac{dU}{dz} w + \frac{\partial \phi}{\partial x} = 0, \quad (1)$$

$$\frac{\partial \phi}{\partial z} = b, \quad (2)$$

$$U \frac{\partial b}{\partial x} + N^2 w = \frac{gQ}{c_p T_0}, \quad (3)$$

$$\frac{\partial u}{\partial x} + \frac{\partial w}{\partial z} = 0. \quad (4)$$

Here, u and w are the perturbation horizontal and vertical velocities, respectively, ϕ the perturbation kinematic pressure ($=p/\rho_0$, where p is the perturbation pressure and ρ_0 the basic-state density), b the perturbation buoyancy ($=g\theta/\theta_0$, where g is the gravitational acceleration, θ the perturbation potential temperature, and θ_0 the reference potential temperature), U the basic-state wind in the x -direction, N the buoyancy frequency, T_0 the basic-state temperature, c_p the specific heat of air at constant pressure, and Q the diabatic forcing. Equations (1)–(4) are the horizontal momentum equation in the x -direction, the hydrostatic equation, the thermodynamic energy equation, and the mass continuity equation, respectively. The above four equations can be combined into a single equation for the perturbation vertical velocity of

$$U^2 \frac{\partial^2 w}{\partial z^2} - U \frac{d^2 U}{dz^2} w + N^2 w = \frac{gQ}{c_p T_0}. \quad (5)$$

Taking the Fourier transform of (5) in x gives

$$\frac{\partial^2 \hat{w}}{\partial z^2} + \left[\frac{N^2}{U^2} - \frac{1}{U} \frac{d^2 U}{dz^2} \right] \hat{w} = \frac{g\hat{Q}}{c_p T_0 U^2}. \quad (6)$$

We consider a two-layer atmosphere, which is sketched in Fig. 1. The basic-state wind has a constant shear up to $z=z_1$ (region 1) and is constant above (region 2). There exists a critical level (wind reversal level) in region 1. The buoyancy frequency is assumed to be piecewise constant in each layer. Diabatic forcing is confined from $z=0$ to $z=d$ in region 1. Then,

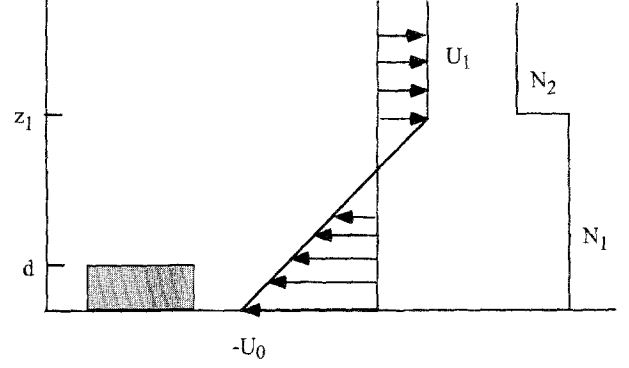


Fig. 1. A schematic diagram of a two-layer atmosphere. The symbols d and z_1 represent the heights of the cooling top and shear layer top, respectively. U_0 is the magnitude of the surface wind, U_1 is the wind speed in the constant wind layer, and N_1 and N_2 are buoyancy frequencies of the shear layer and constant wind layer, respectively

(6) in each region can be written as

$$\frac{\partial^2 \hat{w}_1}{\partial z^2} + \frac{\text{Ri}}{(z - z_c)^2} \hat{w}_1 = \frac{g\hat{Q}}{c_p T_0 \alpha^2 (z - z_c)^2} \quad \text{for } 0 \leq z < d, \quad (7)$$

$$\frac{\partial^2 \hat{w}_1}{\partial z^2} + \frac{\text{Ri}}{(z - z_c)^2} \hat{w}_1 = 0 \quad \text{for } d \leq z < z_1, \quad (8)$$

$$\frac{\partial^2 \hat{w}_2}{\partial z^2} + \frac{N_2^2}{U_1^2} \hat{w}_2 = 0 \quad \text{for } z \geq z_1. \quad (9)$$

Here, Ri denotes the Richardson number defined by $\text{Ri} = N_1^2/\alpha^2$, where $\alpha = (U_0 + U_1)/z_1$. The height of the critical level is $z_c = U_0/\alpha$. Note that U_0 is the magnitude of the surface wind and U_1 is the wind speed at $z=z_1$. Then, the solution in each region is given by

$$\hat{w}_1(k, z) = A_1(z - z_c)^{1/2+i\mu} + B_1(z - z_c)^{1/2-i\mu} + \frac{g\hat{Q}}{c_p T_0 N_1^2} \quad \text{for } 0 \leq z < d, \quad (10)$$

$$\hat{w}_1(k, z) = A_2(z - z_c)^{1/2+i\mu} + B_2(z - z_c)^{1/2-i\mu} \quad \text{for } d \leq z < z_1, \quad (11)$$

$$\hat{w}_2(k, z) = A_3 e^{i\lambda(z-z_1)} + B_3 e^{-i\lambda(z-z_1)} \quad \text{for } z \geq z_1. \quad (12)$$

Here, A_1 , B_1 , A_2 , B_2 , A_3 , and B_3 are unknown coefficients of k , which can be determined by

proper boundary and interface conditions, and $\mu = (\text{Ri} - 1/4)^{1/2}$ and $\lambda = U_1/N_2$. There exists a branch point at $z = z_c$ in this solution. We pick up the branch $(z - z_c) = |z - z_c|$ for $z > z_c$ and $(z - z_c) = |z - z_c|e^{-i\pi}$ for $z < z_c$ from causality (Booker and Bretherton, 1967). We assume a flat surface, which requires $\hat{w}_1 = 0$ at $z = 0$ as a lower boundary condition. For the upper boundary, we use the radiation condition which permits wave energy to propagate upward (Booker and Bretherton, 1967). The interface conditions at $z = d$ appears to be that both \hat{w} and $\partial\hat{w}/\partial z$ are continuous across the interface. At the interface between the different regions in Fig. 1, we require the continuity of vertical velocity and pressure. Thus, the interface conditions at $z = z_1$ can be written as

$$\hat{w}_2 = \hat{w}_1, \quad (13)$$

$$\frac{\partial\hat{w}_2}{\partial z} = \frac{\partial\hat{w}_1}{\partial z} - \frac{\hat{w}_1}{z_1 - z_c}. \quad (14)$$

Then, we have two boundary conditions and four interface conditions. Therefore, the six unknown coefficients in (10)–(12) can be determined (the six coefficients are given in Appendix) and the perturbation vertical velocity in each region can be obtained analytically in wavenumber space. Then, the perturbation vertical velocity in physical space can be obtained by performing the inverse Fourier transform. Solutions for other variables (u , ϕ , and b) can be obtained through (1)–(4).

2.2 Flow Response to a Prescribed Heat Sink

We consider the diabatic forcing given by

$$Q(x, z) = \begin{cases} Q_0 \left[\frac{a_1^2}{x^2 + a_1^2} - \frac{a_1 a_2}{x^2 + a_2^2} \right] & \text{for } 0 \leq z \leq d, \\ 0 & \text{elsewhere,} \end{cases} \quad (15)$$

where Q_0 is the magnitude of diabatic forcing (negative for cooling) and a_1 the half-width of the bell-shaped function. The second term with a_2 represents a compensated forcing, which is included to avoid a net forcing problem in an inviscid, steady-state fluid system (Smith and Lin, 1982).

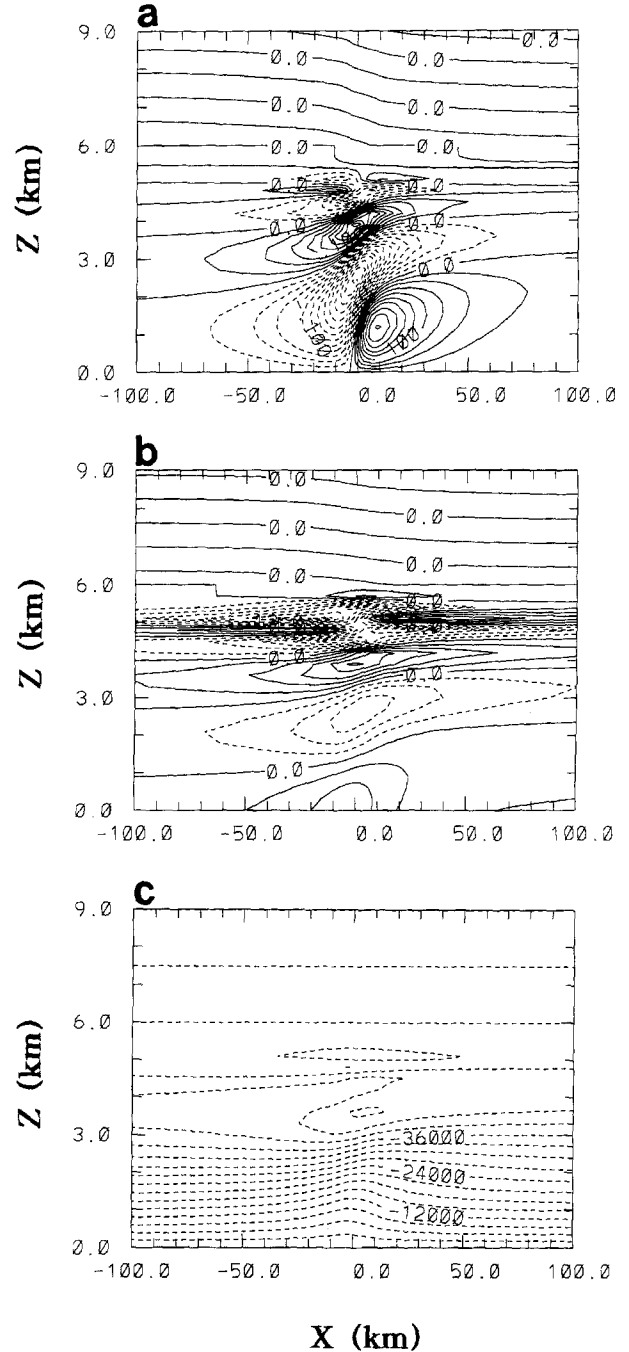


Fig. 2. The linear, steady-state solution fields of (a) the perturbation vertical velocity, (b) the perturbation horizontal velocity, and (c) the total streamfunction. The parameters considered are $d = 2$ km, $z_1 = 6$ km, $U_0 = 18$ m s⁻¹, $U_1 = 2$ m s⁻¹, $N_1 = 0.015$ s⁻¹, $N_2 = 0.01$ s⁻¹, $a_1 = 10$ km, $a_2 = 50$ km, $T_0 = 273$ K, and $Q_0 = -2$ J kg⁻¹ s⁻¹. The contour intervals in (a), (b), and (c) are 0.025 m s⁻¹, 3 m s⁻¹ and 3000 m² s⁻¹, respectively

Figure 2 shows the fields of the perturbation vertical and horizontal velocities and total streamfunction. From the mass continuity Eq. (4), we can define the perturbation streamfunc-

tion φ which satisfies the relationships of $\partial\varphi/\partial x = -w$ and $\partial\varphi/\partial z = u$. Then, the total streamfunction can be obtained by

$$\varphi_t(x, z) = \int_0^z U(z)dz - \int w(x, z)dx. \quad (16)$$

The parameters considered in Fig. 2 are $d = 2$ km, $z_1 = 6$ km, $U_0 = 18$ m s⁻¹, $U_1 = 2$ m s⁻¹, $N_1 = 0.015$ s⁻¹, $N_2 = 0.01$ s⁻¹, $a_1 = 10$ km, $a_2 = 50$ km, $T_0 = 273$ K, and $Q_0 = -2$ J kg⁻¹s⁻¹. With these parameters, the Richardson number associated with the basic-state flow is 20.25 and a critical level appears at $z = 5.4$ km.

Below the critical level, there exist a strong updraft on the upstream side of the specified cooling and a compensating downdraft on the downstream side of the cooling. Because the waves are attenuated by a factor of $e^{-\pi\mu}$ across the critical level when the Richardson number associated with the basic-state flow is larger than 1/4, almost no perturbations exist above the critical level. However, the upstream phase tilt of the wave appears above the critical level, indicating an upward energy propagation, even though its amount is very small. The magnitude and structure of the updraft on the upstream side of the specified cooling are determined by the relative magnitudes among the basic-state wind (U), the speed of cold outflow propagating upstream [$c_d = \{Q_0 g a_1 d / (c_p T_0)\}^{1/3}$], and the horizontal speed of dominant gravity waves ($c_w = Nd/\pi$) (Lin and Chun, 1991). For the parameters used in Fig. 2, c_d and c_w are 11.3 m s⁻¹ and 9.5 m s⁻¹, respectively.

In the perturbation horizontal velocity field, the maximum horizontal perturbation near the critical level exceeds the basic-state wind speed. This obviously violates the linear assumption. Note that the linear assumption near the critical level breaks down because the vertical wavelength becomes zero and the perturbation horizontal velocity becomes infinity as the wave approaches the critical level. The total streamfunction field shows the wave overturning near the critical level because of the strong perturbation horizontal velocity there. Above the critical level, almost no wave propagation can be seen because the wave energy is absorbed near the critical level for $Ri > 1/4$.

Figure 3 shows the domain maximum perturbation vertical velocity as a function of the

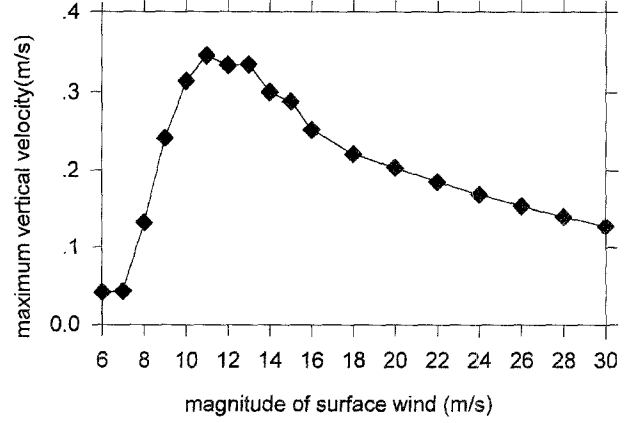


Fig. 3. The domain maximum perturbation vertical velocity as a function of the magnitude of the surface wind in the linear, steady-state solution. The parameters considered are the same as in Fig. 2

magnitude of the surface wind. Because the shear layer depth and the basic-state wind at $z = z_1$ are fixed, stronger surface wind means stronger wind shear. Three flow regimes may be identified in Fig. 3. For $U_0 < 11$ m s⁻¹, the maximum vertical velocity increases with increasing wind shear. For $U_0 > 14$ m s⁻¹, the maximum vertical velocity decreases with increasing wind shear. Between $U_0 = 11$ m s⁻¹ and 14 m s⁻¹, the maximum vertical velocity remains almost unchanged. In fact, these three flow regimes are related to the relative magnitudes among U_0 , c_w , and c_d . The basic-state wind with $U_0 = 11.8$ m s⁻¹ is just opposed by c_w if we consider the averaged basic-state wind from the surface to the top of the specified cooling. That is, for $U_0 < 11.8$ m s⁻¹, gravity waves can propagate upstream against the basic-state wind. Similarly, the basic-state wind with $U_0 = 14.0$ m s⁻¹ is just opposed by c_d . Thus, for $U_0 > 14$ m s⁻¹, the density current cannot propagate upstream against the basic-state wind. When the basic-state wind speed is larger than the density current speed, the domain maximum vertical velocity decreases as the wind shear increases. This is because a large portion of the specified cooling is used to compensate for the positive vorticity associated with the positive wind shear and the effective cooling used to produce vertical velocity is reduced. The present results in the non-constant shear case are essentially the same as those in the uniform shear case by Lin and Chun (1991).

3. Numerical Simulations

In this study, two numerical simulations (dry and moist) are conducted. The dry simulation is performed using gravity wave solutions obtained in the theoretical part as initial conditions. During the time integration, the diabatic cooling given by (15) is included. The moist simulation is performed using the quasi-steady perturbations produced in the dry simulation as initial conditions. This gives model-consistent initial conditions.

3.1 Numerical Model

The numerical model used in this study is the ARPS (Advanced Regional Prediction System) developed at the CAPS (Center for Analysis and Prediction of Storms) (Xue et al., 1995) of the University of Oklahoma. The ARPS is a 3-dimensional, nonhydrostatic, compressible finite-difference model that includes explicit liquid-ice phase cloud processes. In this study, two-dimensional (x - z) simulations are performed. The ice phase cloud processes and surface processes are excluded and the rotational

effect of the Earth is neglected in our simulations. The model domain is 200 km wide and 21 km high with a horizontal resolution of 1 km and a vertical resolution of 300 m. Radiation boundary conditions proposed by Orlanski (1976) and Klemp and Durran (1983) are used at the model lateral and top boundaries, respectively.

3.2 Dry Simulation

In the dry simulation, the response of an atmosphere to specified cooling is investigated using the linear, steady-state gravity wave solutions as initial conditions. The center of the specified cooling with the same structure as that in the theoretical part is located at $x = 60$ km. The basic state wind profile used in the numerical simulations is also the same as that in the theoretical part. The basic-state temperature profile used in the numerical simulations is shown in Fig. 6a.

Figure 4 shows the time series of the domain maximum and minimum perturbation vertical velocity (Fig. 4a) and perturbation pressure (Fig. 4b). The domain maximum vertical velocity

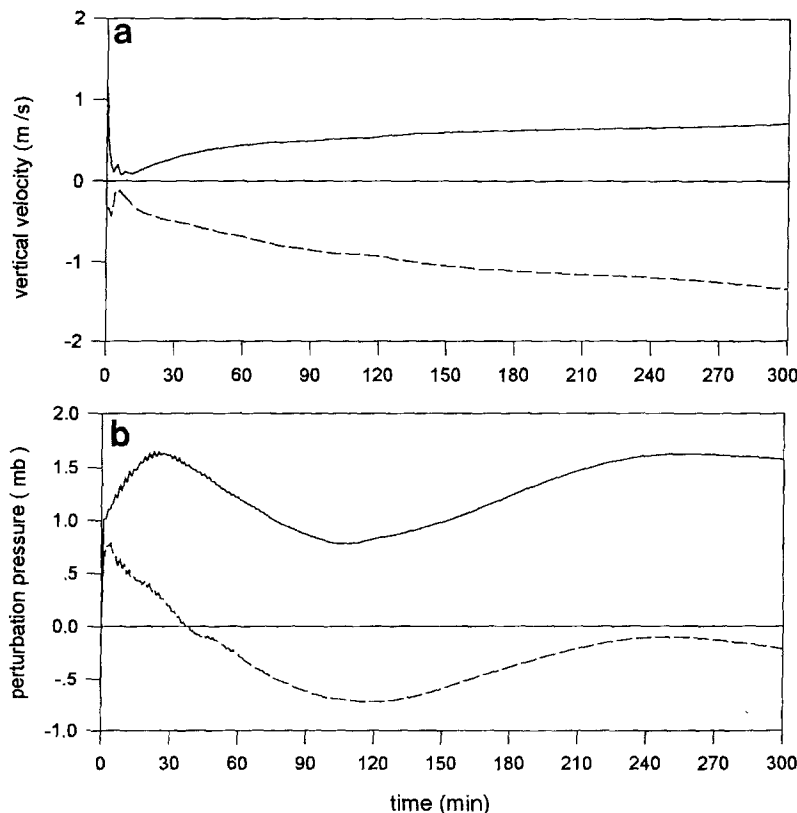


Fig. 4. The time series of the domain maximum (solid line) and minimum (dashed line) (a) perturbation vertical velocity and (b) perturbation pressure in the dry model simulation

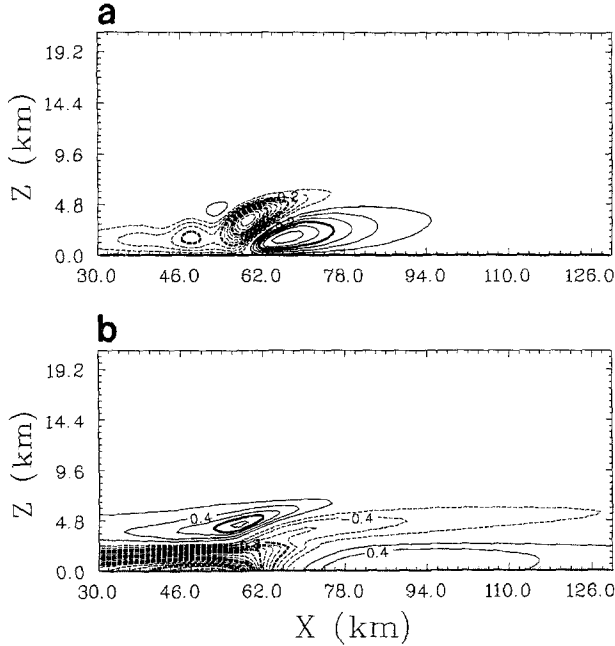


Fig. 5. The fields of (a) the perturbation vertical velocity and (b) the perturbation potential temperature at $t = 4$ h in the dry model simulation. The contour intervals in (a) and (b) are 0.1 m s^{-1} and 0.2 K , respectively

remains almost constant after $t \sim 180$ min, while the domain minimum vertical velocity decreases gradually. The maximum perturbation pressure increases after $t \sim 115$ min and remains almost constant after $t \sim 240$ min. Based on the domain maximum perturbation vertical velocity and perturbation pressure, we consider that the time of $t = 4$ h is in the quasi-steady state.

Figure 5 shows the perturbation vertical velocity and perturbation potential temperature fields at $t = 4$ h. Only a portion of the horizontal domain, from $x = 30$ to 130 km, is shown. There exist an updraft on the upstream side of the specified cooling with a maximum value of 0.65 m s^{-1} and a downdraft with a minimum of -1.19 m s^{-1} . Because in this case the nonlinearity factor of thermally-induced internal gravity waves, as defined by $\mu' = gQ_0a_1/(c_pT_0NU^2)$ in Chun (1991), is small (~ 0.2), the nonlinear response is similar to the linear, steady-state response. However, there are virtually no waves with small vertical wavelengths near the critical level. This implies that a vertical resolution of 300 m is not enough to resolve waves near the critical level, even though this vertical resolution might be good for simulating mesoscale convective system.

The perturbation potential temperature is negative near the surface on the downstream side of the specified cooling. Density current propagating upstream does not develop. As mentioned earlier, the magnitude of gravity waves or perturbation potential temperature depends on the relative magnitudes between the basic-state wind shear and the theoretical density current speed (c_d). In this case, the large positive wind shear in the lower layer reduces the effective cooling to produce negative perturbation potential temperature or positive perturbation wind propagating upstream against the basic-state wind.

3.3 Moist Simulation

Figure 6 shows the basic-state wind and thermodynamic profiles used in the numerical simulations. The thermodynamic sounding (Fig. 6a) is an analytical one given by Weisman and Klemp (1982), which represents a favorable condition for midlatitude squall lines. In this sounding, the convective available potential energy (CAPE) considering the effect of negative buoyancy due to liquid water is about $2888 \text{ m}^2 \text{ s}^{-2}$. This amount of CAPE is enough to produce a severe convective system. The basic-state wind profile (Fig. 6b) is the same as that used in the theoretical part. Figure 6c shows the buoyancy frequency profile calculated using the temperature profile in Fig. 6a. Below the tropopause ($\sim 12 \text{ km}$), the buoyancy frequency is $\sim 0.006 \text{ s}^{-1}$ and above the tropopause it is $\sim 0.02 \text{ s}^{-1}$. In the moist simulation, convection is initiated by the model-consistent quasi-steady gravity waves. The numerical integration is carried out for 4 hours.

Figure 7 shows the time series of the domain maximum and minimum perturbation vertical velocity and the domain maximum water vapor mixing ratio (q_v), cloud water mixing ratio (q_c), and rain water mixing ratio (q_r). The maximum vertical velocity increases during the first 40 min or so and then starts to oscillate. The rain water is produced after $t = 25$ min. The rain water mixing ratio shows its first maximum at $t = 37$ min and second maximum at $t = 60$ min. Then, the rain water mixing ratio decreases and oscillates. The evolution pattern of the maximum cloud water mixing ratio is similar to that of the maximum

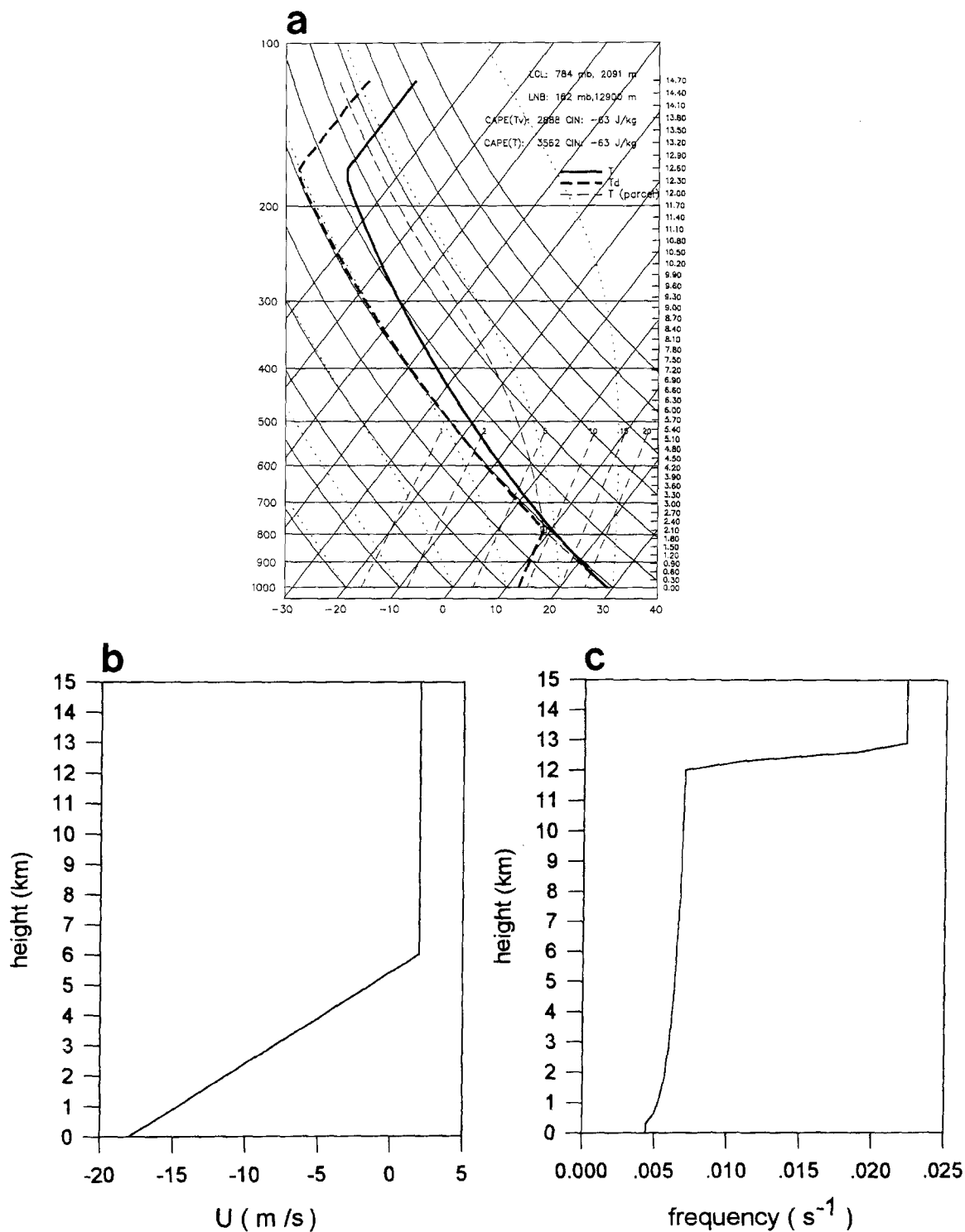


Fig. 6. (a) The skew T -log p diagram of the basic-state thermodynamic sounding, (b) the basic-state wind profile, and (c) the calculated basic-state buoyancy frequency profile

rain water mixing ratio with several minutes of time lag, even though the magnitude and variation of the maximum cloud water mixing ratio are smaller than those of the maximum rain water mixing ratio. We divide the storm devel-

opment into two stages for the subsequent presentation – the first stage before 90 min and the second stage between 90 min to 180 min. The storm evolution during each stage will be shown in Figs. 9–11 and Figs. 12–14, respectively.

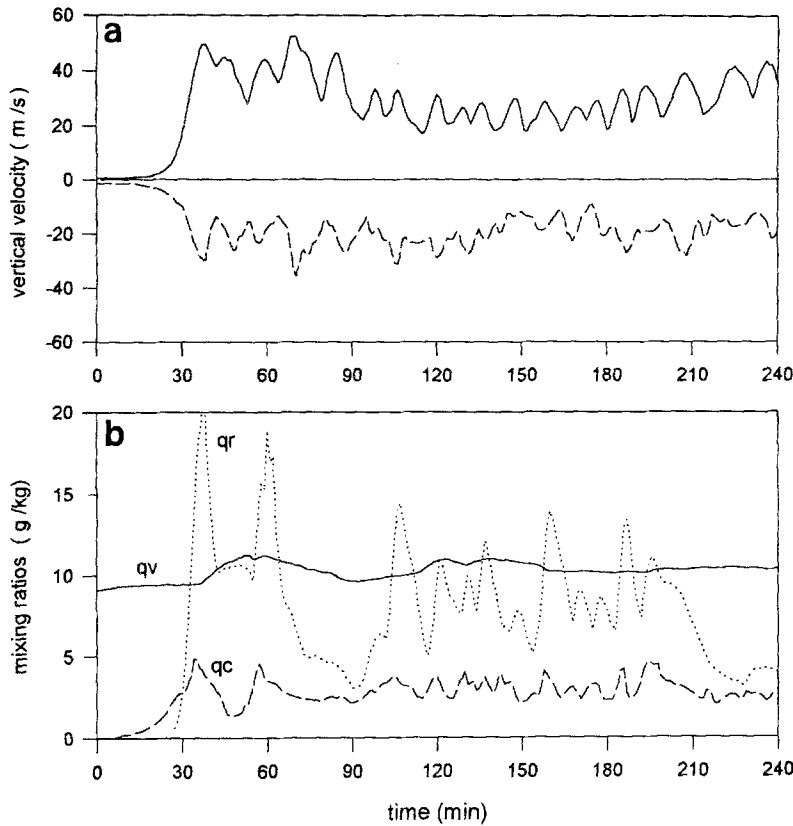


Fig. 7. The time series of (a) the domain maximum (solid line) and minimum (dashed line) perturbation vertical velocity and (b) the domain maximum water vapor mixing ratio (q_v) (solid line), cloud water mixing ratio (q_c) (dashed line), and rain water mixing ratio (q_r) (dotted line) in the moist model simulation

Figure 8 shows the power spectra of the domain maximum perturbation vertical velocity and rain water mixing ratio. The time series data of Fig. 7a and 7b for $t \geq 30$ min (after convection develops) are used to construct Fig. 8. The data are detrended before taking the Fourier transform for the spectral analysis. In the perturbation vertical velocity spectrum, there are three dominant peaks with oscillation periods of 12.1, 15.1, and 17.1 min. In the rain water mixing ratio spectrum, 12.1, 25.6, and 51.2 min are dominant peak oscillation periods. The peak in the 12.1 min period in both the power spectra is related to the oscillation at the second stage. The other two main peaks are different with each other. This is mainly because in the development stage before 90 min the time evolution of the vertical velocity is different from that of the rain water mixing ratio. Fovell and Dailey (1995) performed the spectrum analysis of the domain maximum vertical velocity at the mature stage for the cases of different shear layer depths. They used the unfiltered time series data and the significance of spectral peaks was checked by red noise threshold.

Figure 9 shows the evolution of the perturbation vertical velocity field from $t = 46.5$ min to $t = 69$ min in a time interval of 2.5 min. This time period belongs to the first stage. There are approximately two oscillation periods during this time in Fig. 9. Only a portion of the horizontal domain (from $x = 30$ km to 90 km) including a major updraft is shown in Figs. 9–11. At $t = 46.5$ min, there is a strong updraft at $x \sim 56$ km that extends to $z \sim 15$ km. Above this height, gravity waves induced by convection impinging the stably stratified stratosphere propagate upward. Note that the basic-state wind blows from the right to the left below $z = 6$ km and reverses its direction above it. At $t = 46.5$, 49, and 51.5 min, the updraft is tilted slightly upshear in the lower layer and downshear in the upper layer. This is because the cold pool does not develop fully enough to overcome the positive vorticity associated with the basic-state wind shear. As time passes, a new cell (cell 2) develops on the upstream side of the major cell (cell 1). Cell 2 intensifies as it moves slightly downstream and then replaces cell 1 as a major updraft. Cell 1 decays as cell 2 intensifies

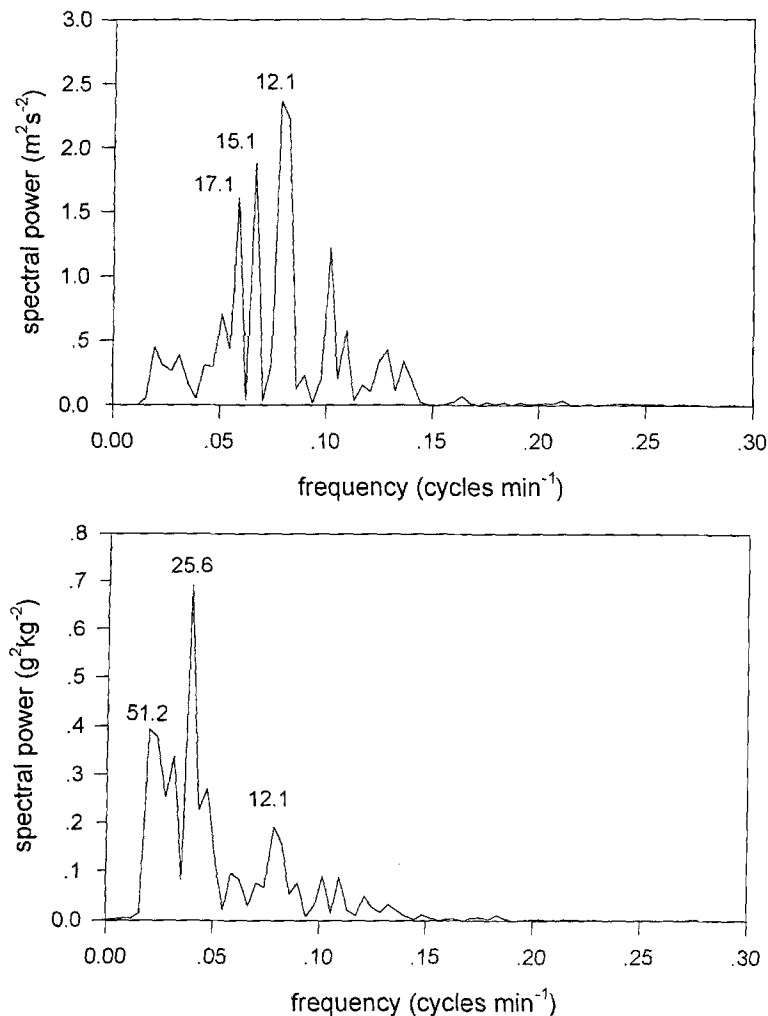


Fig. 8. The power spectra of (a) the domain maximum perturbation vertical velocity in Fig. 7a and (b) the domain maximum rain water mixing ratio in Fig. 7b after $t=30$ min in the moist model simulation. The data are detrended before taking the Fourier transform for the spectral analysis. Significant peaks in each spectrum are indicated in numeric values in the unit of min

because the warm and humid inflow blowing from the front into the storm is prevented by cell 2. This cut-off process is one of the characteristics of multicell storm (Houze, 1993). As time continues, cell 2 intensifies and reaches a second maximum in the vertical velocity for the two oscillation periods at $t=59$ min. The major updraft at $t=59$ min clearly shows the upshear tilt of the updraft, indicating the mature stage of the storm. After this, the cold pool in the lower layer develops and propagates upstream against the inflow. This is the stage of density current. As the strength of the cold pool in the lower layer increases, the negative vorticity by the cold pool dominates the positive vorticity due to the basic-state wind. Updraft at the head of the density current develops at this stage and becomes separated from the major updraft.

Figure 10 shows the wind vector field superimposed on the cloud water mixing ratio field,

which corresponds to Fig. 9. At $t=46.5$ and 49 min, the updraft and cloud are almost upright. As time passes, cell 2 develops at the upstream of the major cloud cell. At $t=51.5$ min, cell 2 becomes a primary cell and develops at $t=59$ min with a maximum mixing ratio during the time period shown in Fig. 10. At $t=59$ min, the updraft and cloud show upshear tilt. Also, an anvil cloud is observed in the wind vector field, which is not shown in the cloud water mixing ratio field because the contour is from 0.25 kg^{-1} . After this time, inflow from the front of the storm in the lower layer to the rear side of the storm in the upper layer, named the front-to-rear (FTR) flow, and inflow from the rear of the storm in the middle level to the down of the cold pool, named the rear-to-front (RTF) flow, are clearly observed. Especially, relatively cold and dry RTF inflow enhances the strength of the cold pool that is a major

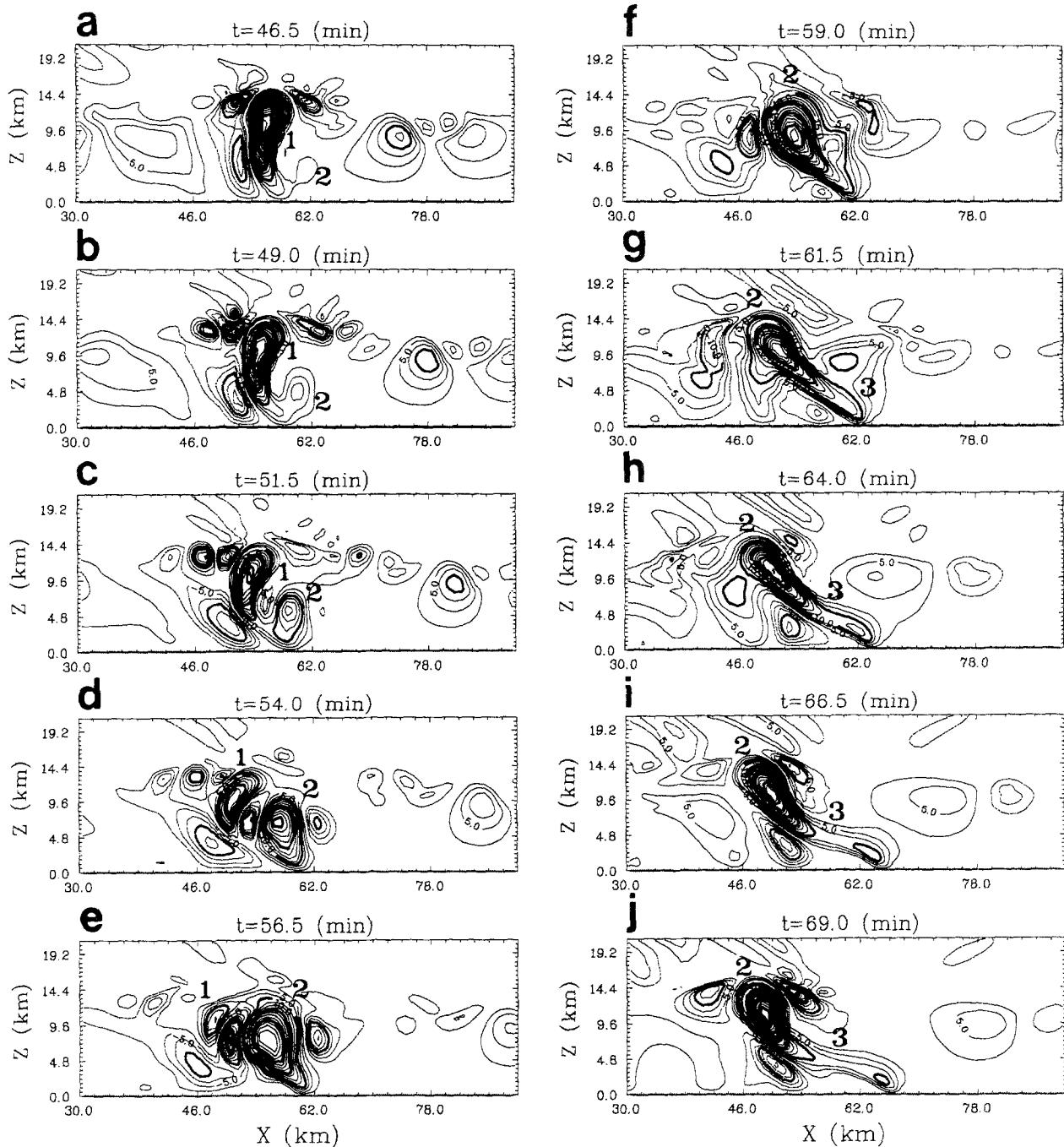


Fig. 9. The evolution of the perturbation vertical velocity field from $t = 46.5$ min to $t = 69$ min in a time interval of 2.5 min in the moist model simulation. The contour interval is 2.5 m s^{-1}

engine to sustain multicell storm (Rotunno et al., 1988).

Figure 11 shows the horizontal velocity, perturbation pressure, perturbation potential temperature, and equivalent potential temperature fields at $t = 59$ min corresponding to Fig. 9f. The maximum and minimum horizontal velocities are located in the upper troposphere. The FTR inflow and RTF inflow are clearly seen at

this time. The leftward-blowing wind in the upper troposphere as a part of the FTR inflow and the rightward-blowing wind below as a part of the RTF inflow at the center of the major convection produce the negative horizontal vorticity. This vorticity causes a mesolow at the storm center as a dynamical source of the pressure perturbation. In the mesoscale convective system producing strong horizontal and

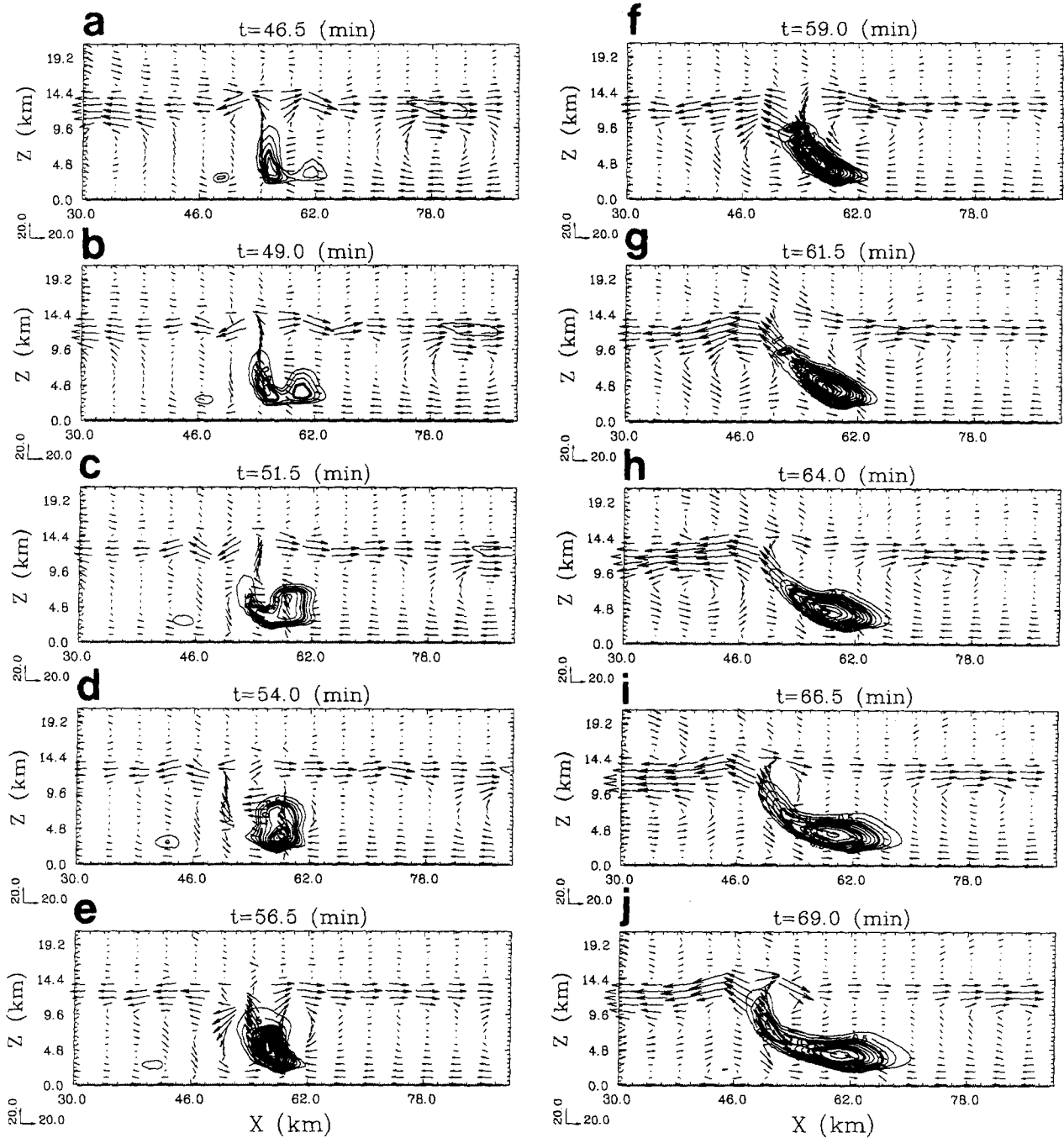


Fig. 10. The same as in Fig. 9 except for the wind vector field superimposed on the cloud water mixing ratio field in the moist model simulation. The contour interval of the cloud water mixing ratio is 0.25 g kg^{-1} .

vertical winds, the pressure perturbation is induced mainly by a dynamical source rather than a buoyancy source (Houze, 1993). The cold pool in the lower layer is represented by the negative perturbation potential temperature. At this time, the cold outflow is not propagating upstream against the inflow. At the center of the convection, there is a warming of about 16 K by the latent heating due to convection. Near the

cloud top, large cooling appears mainly due to the evaporation and the adiabatic process by updraft. In this study, radiative process is not included. The equivalent potential temperature is a conservative variable in the moist atmosphere except for the cross-over zone. The thermodynamic sounding in Fig. 6a represents a conditionally unstable atmosphere below $z \sim 6$ km. That is, 6 km-deep, warm and humid air enters

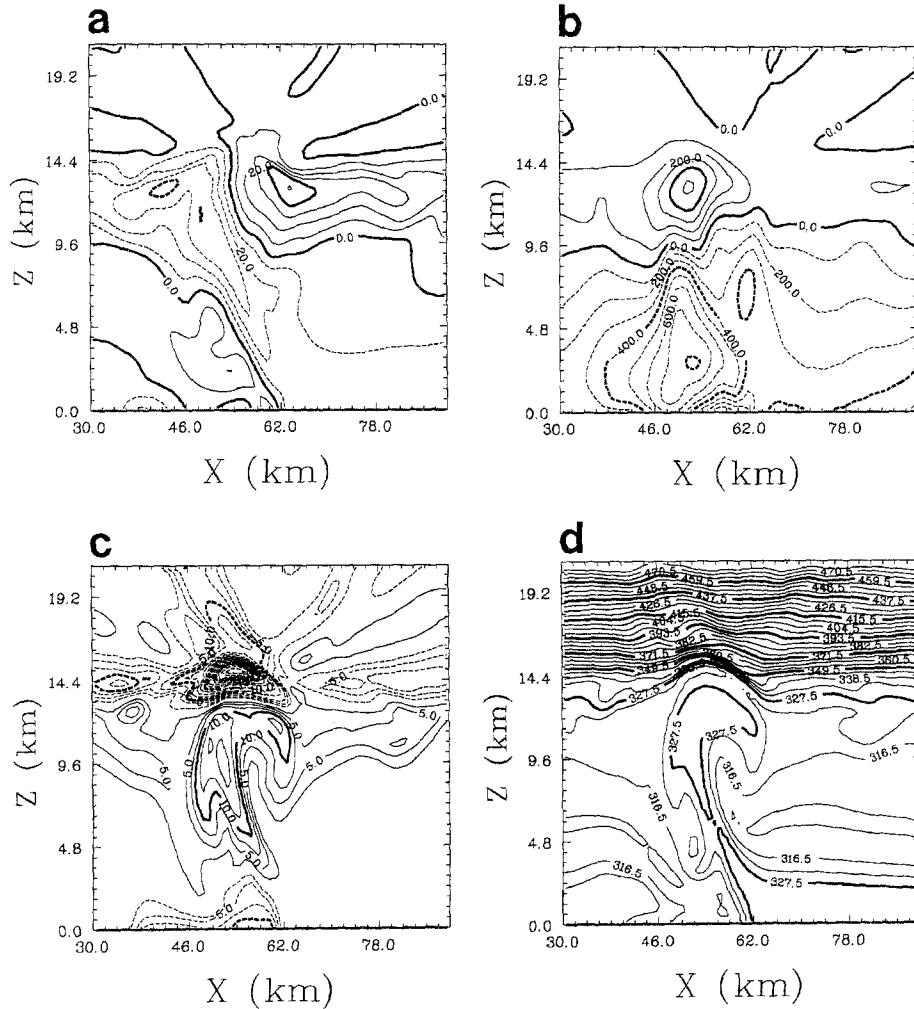


Fig. 11. The fields of (a) the horizontal wind, (b) the perturbation pressure, (c) the perturbation potential temperature, and (d) the equivalent potential temperature at $t=59$ min corresponding to Fig. 9f in the moist model simulation. The contour intervals in (a)–(d) are 10 m s^{-1} , 100 Pa , 2.5 K , and 5.5 K , respectively

the storm. Since the equivalent potential temperature near the surface is higher than that near $z=6 \text{ km}$, the surface air goes into the storm over the cold pool, while the relatively cold air near $z=6 \text{ km}$ slides down the storm and enhances the cold pool. This process of lifting warm air and sliding down cold air makes the air stabilize.

Figure 12 shows the evolution of the perturbation vertical velocity field from $t=136 \text{ min}$ to $t=158 \text{ min}$ in a time interval of 2.75 min . This time period belongs to the second stage. The horizontal domain shown in Figs. 12 and 13 is from $x=40 \text{ km}$ to 100 km . At $t=136 \text{ min}$, there exist a main updraft located at $x \sim 67 \text{ km}$ and compensating downdrafts on the upshear and downshear sides. Near $x=90 \text{ km}$, there exists another updraft, marked by G, in the lower layer, which is produced by the convergence of the cold

air from the cold pool and the warm and humid air entering the storm from the right. This updraft resembles somewhat the steady-state, linear gravity waves induced by the specified cooling in the theoretical part. At $t=136 \text{ min}$, cell 2 starts to form in the lower layer between the major updraft and the updraft at the head of the density current. As time continues, cell 2 develops as it moves downstream and becomes a primary cell at $t=141.5 \text{ min}$. Cell 2 intensifies until $t=147 \text{ min}$ and a new cell (cell 3) appears and develops between $t=149.75$ and $t=158 \text{ min}$. This process is repeated at later times. The magnitude of the updraft is maximized when a new primary cell is at the mature stage. Once another new cell forms and develops, the maximum updraft diminishes during an oscillation period.

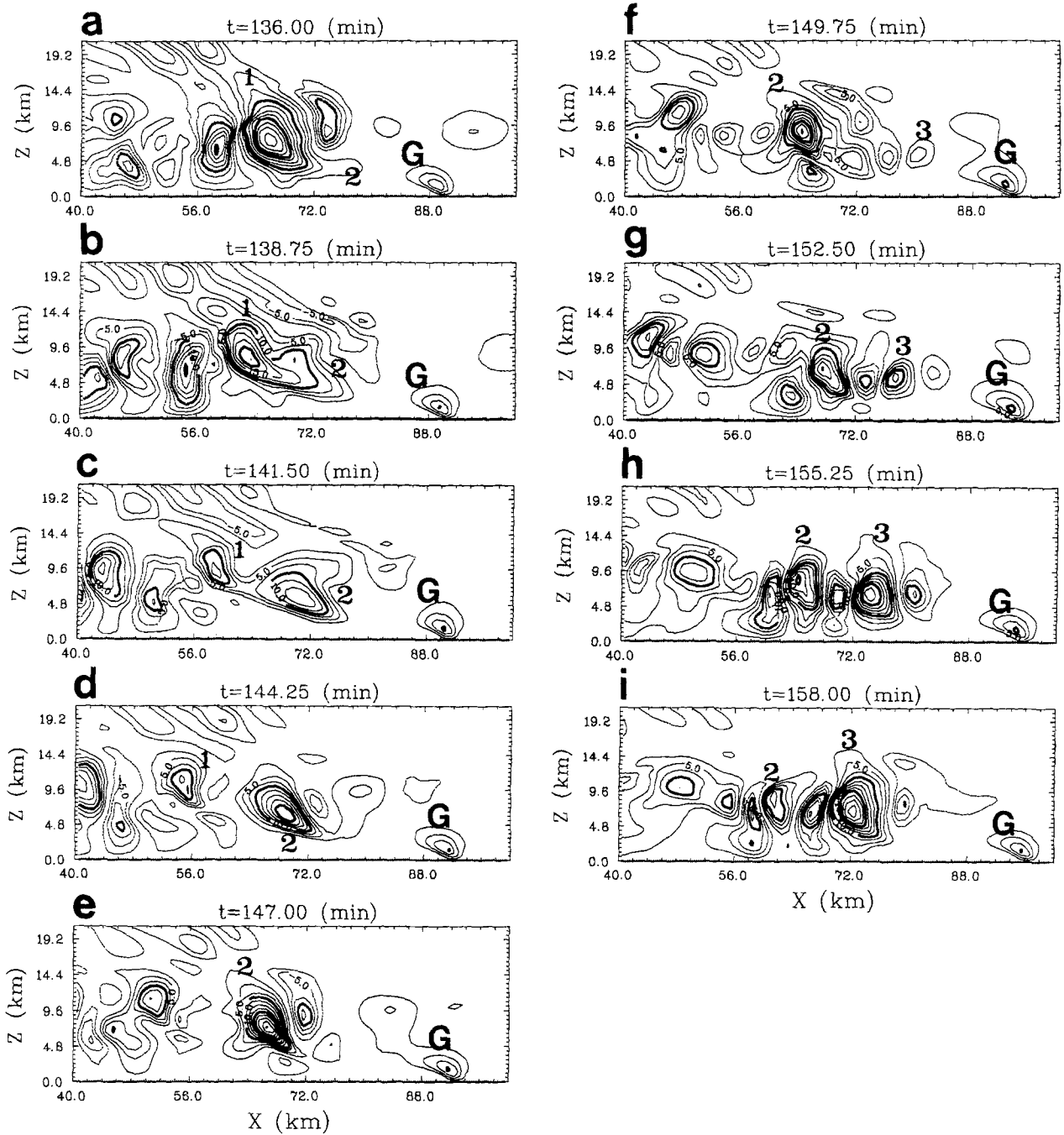


Fig. 12. The evolution of the perturbation vertical velocity field from $t = 136$ min to $t = 158$ min in a time interval of 2.75 min in the moist model simulation. The symbol G indicates the updraft at the gust front. The contour interval is 2.5 m s^{-1}

The above-mentioned process is also observed in the wind vector field superimposed on the cloud water mixing ratio field (Fig. 13). The existence of a cloud between the major updraft and the updraft at the gust front is clearly shown in the cloud water mixing ratio field. The cloud field is much tilted upshear because the cold pool is strong at this time. An anvil cloud is also observed in the cloud water mixing ratio field. As

time passes, cell 2 located between the primary cloud cell and that at the density current head develops further and becomes a primary cell. At $t = 149.75$ min, the cloud cell is separated by two parts, one located at the leading edge of the convective system and the other located at the center of the domain. Once the new cell develops, the warm and humid air entering the front of the convection raises the cell, while the

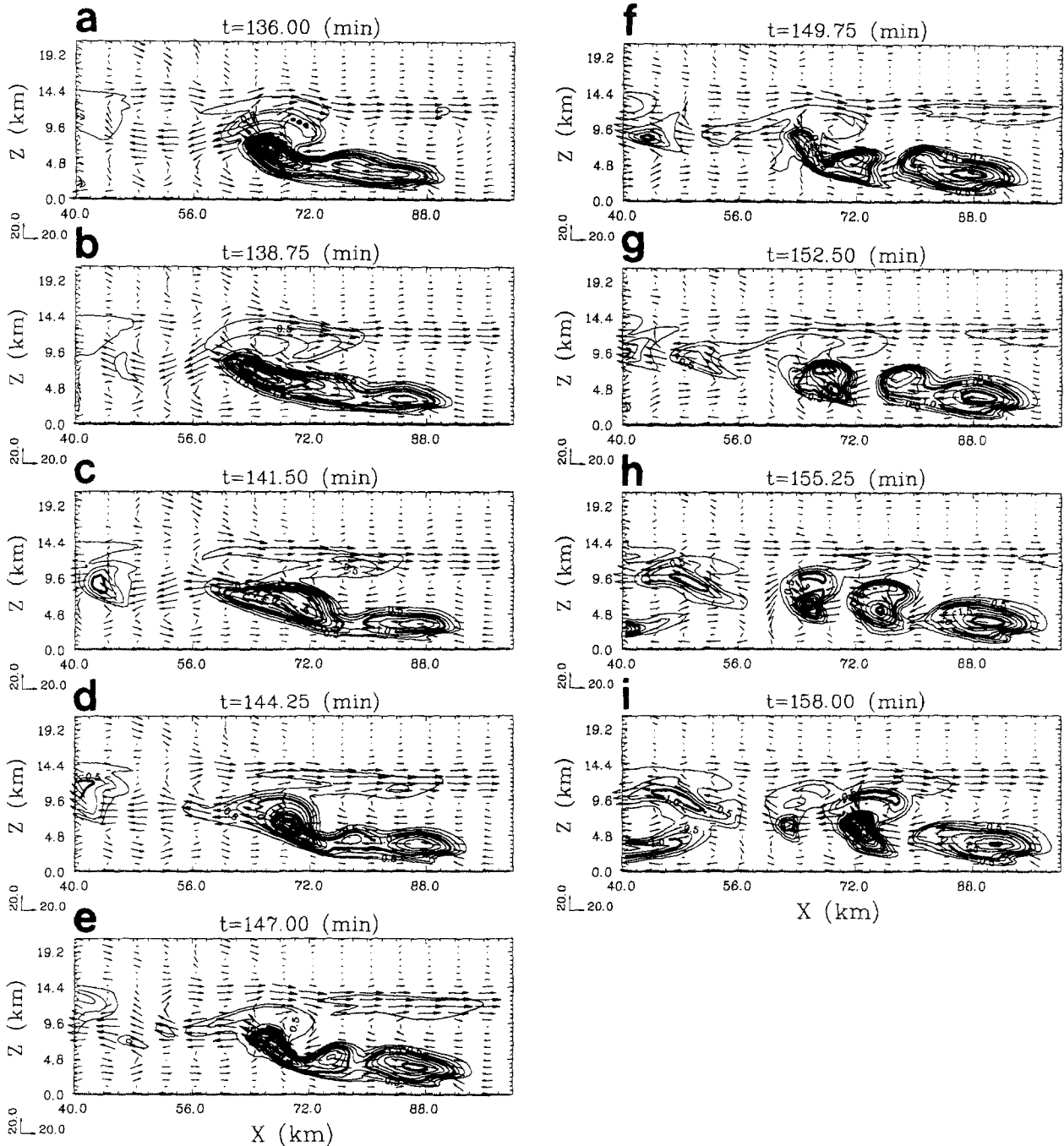


Fig. 13. The same as in Fig. 12 except for the wind vector field superimposed on the cloud water mixing ratio field in the moist model simulation. The contour interval of the cloud water mixing ratio is 0.25 g kg^{-1}

old cell is separated from the new cell by the energy cut-off process. This process is repeated again as long as the new cell can be continuously produced.

Yang and Houze (1995) suggested that new cells are gravity waves induced by the gust front updraft and that they propagate downstream relative to the density current. They showed that the phase relationship of the simulated flow fields

is consistent with that of linear, monochromatic gravity waves. Lin et al. (1998) carefully analyzed the phase relationship in multicell storms and found that the growing cell and propagating cell should be considered differently. It was shown that the growing cell experiences a critical level in order to amplify and only the propagating cell has the characteristics of gravity waves.

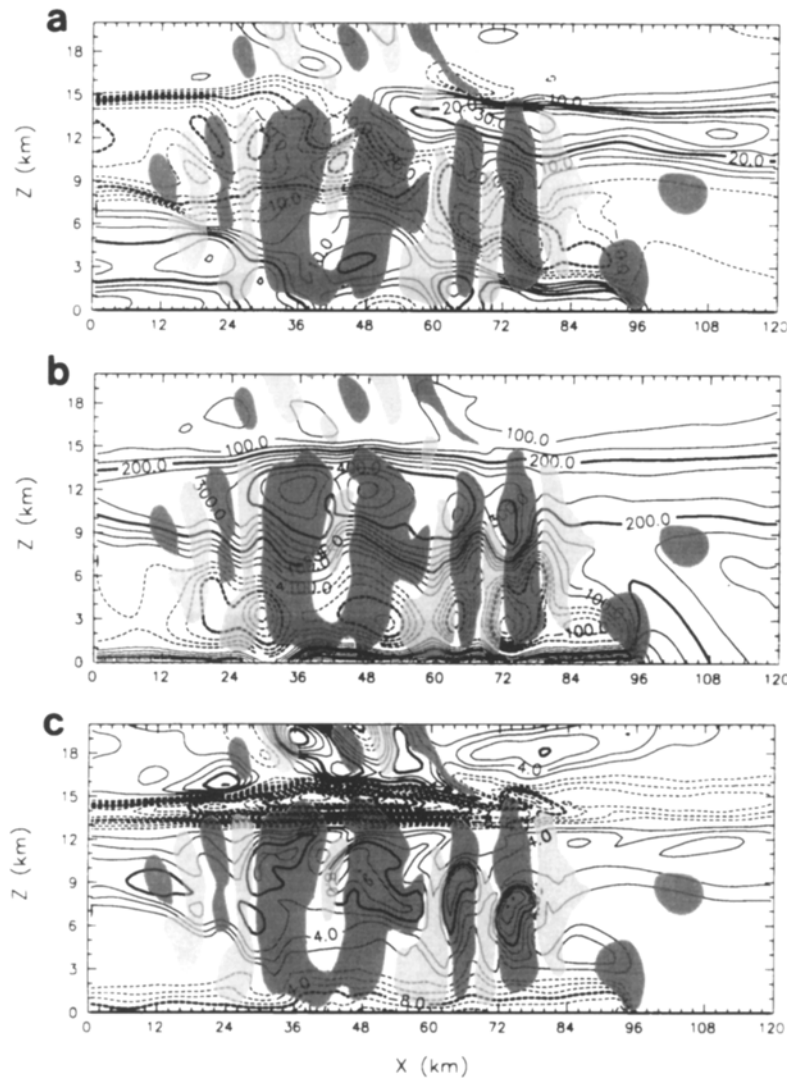


Fig. 14. The vertical velocity fields superimposed on (a) the perturbation horizontal velocity, (b) the perturbation pressure, and (c) the perturbation potential temperature at $t = 149.75$ min corresponding to Fig. 12f. The vertical velocities are dark shaded for $w > 1 \text{ m s}^{-1}$ and light shaded for $w < -1 \text{ m s}^{-1}$. The contour intervals in (a), (b), and (c) are 10 m s^{-1} , 50 Pa , and 2 K , respectively

In order to examine the characteristics of the new cells, the phase relationship of the simulated flow fields is checked following Yang and Houze (1995) and Lin et al. (1998). Figure 14 shows the vertical velocity fields superimposed on the perturbation horizontal velocity, perturbation pressure, and perturbation potential temperature at $t = 149.75$ min corresponding to Fig. 12f. In the lower layer ($z < 5 \text{ km}$), the perturbation horizontal velocity maxima are located one quarter wavelength behind (to the left of) the updrafts for $x > 60 \text{ km}$ and collocated with the updraft near $x = 48 \text{ km}$. In the middle layer ($5 \text{ km} < z < 13 \text{ km}$), the perturbation horizontal velocity minima are collocated with the updrafts for $x > 60 \text{ km}$ and collocated with the downdrafts for $x < 40 \text{ km}$. Above the clouds, the perturbation

horizontal velocity minima are collocated with the updrafts and the perturbation horizontal velocity maxima are collocated with the downdrafts. The phase relationship between the perturbation pressure and the vertical velocity shows that the perturbation pressure minima are located one quarter wavelength behind the updrafts in the lower layer and the perturbation pressure maxima are collocated with the updrafts in the middle layer. The perturbation potential temperature maxima are collocated with the updrafts in the convective region for $x > 60 \text{ km}$ and located behind the updrafts for $x < 60 \text{ km}$. Above the clouds, the perturbation potential temperature maxima are located one quarter wavelength behind the updrafts. It is shown that the phase relationship of the flow fields for

$x > 60$ km is different from that for $x < 60$ km. This is basically consistent with the results in Lin et al. (1998) except that the clouds in the present case are taller (~ 13 km) than theirs (~ 10 km). If we follow their view, the propagating modes for $x < 60$ km have the characteristics of gravity waves, while the growing modes for $x > 60$ km have not.

Even though the phase relationship of the simulated flow fields has been used to check whether the consecutive convective cells are internal gravity waves or not, it should be used qualitatively because the situation for the nonlinear, moist convection is much different from that for the linear, monochromatic free-mode gravity waves.

4. Summary and Conclusions

In this study, we examined some aspects of internal gravity waves in the multicell-type convective system using a linear, steady-state theory and a numerical model. The basic-state wind considered increases linearly from the surface to $z = 6$ km and is constant above it.

In the theoretical part, we considered the two-dimensional, steady-state response of a stably stratified atmosphere to specified cooling representing the evaporative cooling of falling precipitation in the subcloud layer and obtained analytical solutions for the perturbations induced by the cooling. There exist an updraft on the upstream side of the cooling and a downdraft on the downstream side. The magnitude of the updraft is strongly dependent upon the relative magnitudes between the basic-state wind and the speed of the outflow propagating upstream. As the vertical shear of the basic-state wind increases enough, the magnitude of the updraft decreases because a large portion of the specified cooling is used to compensate for the positive vorticity associated with the positive wind shear and the effective cooling used to produce perturbations is reduced.

In the numerical part, the dry and moist simulations were conducted using the two-dimensional, nonhydrostatic, compressible model. In the dry simulation, the steady cooling was specified in the numerical model. Results showed that in the quasi-steady state the simulated field resembles that of the linear,

steady-state solution. This is because the nonlinearity factor of thermally-induced waves in this case is small. In the moist simulation, the quasi-steady perturbations obtained from the dry simulation were used as initial conditions and the temperature and moisture sounding favorable for convective storm were used as the basic-state thermodynamic field. The simulated convection was a multicell-type convective system. At the first stage, the new convective cell develops near the old cell because the cold pool is almost stationary with respect to the upstream, while at the second stage, the new cell develops primarily by the updraft at the head of the density current, which is located far upstream from the main convective cell. The updraft at the head of the density current somewhat resembles the linear, steady-state response of a stably stratified atmosphere to the specified cooling in the theoretical part. The updraft, forced internal gravity waves at the head of the density current is responsible for the initiation of consecutive convective cells that move downstream and develop as a main convective cell.

In this study, we investigated some aspects of internal gravity waves in the multicell-type convective system. It was clearly shown that waves can effectively initiate convection even with small amplitude. At the mature stage when the cold pool dominates the basic-state wind shear and the density current propagates upstream, the updraft at the head of the density current seems to be a major source of producing consecutive new cells. Because this updraft is considered to be forced internal gravity waves induced by diabatic cooling, it could be said that internal gravity waves have a major role not only in the initiation but also in the maintenance of the multicell-type convective system. However, the contribution of waves to the evolution of the convective system was not examined quantitatively in this study. This is under investigation.

In the real atmosphere, waves are changed not only by forcing to generate them but also by the basic-state wind and stability that can be modified by convection itself. Therefore, in order to investigate two-way interactions between convection and waves, varying basic-state wind and stability by convection should be considered. This is also under investigation.

Acknowledgements

The authors are very grateful to anonymous reviewers whose comments helped clarify some points. The first author was partially supported by the Korean Science and Engineering Foundation under Grant 971-0404-013-2 and the Cray Inc. and Systems Engineering Research Institute (SERI) through "97 Cray R&D" grant. Numerical calculations were carried out on the Cray C90 at the SERI.

Appendix: Coefficients in (10)–(12)

$$A_2 = \frac{(X_8 - X_6)(X_1 F_2 + X_3 F_1)}{(X_8 - X_6)(X_3 - X_1) + (X_5 - X_7)(X_2 X_3 - X_1 X_4)}.$$

$$B_2 = A_2 \left(\frac{X_5 - X_7}{X_8 - X_6} \right).$$

$$A_3 = A_2 \left(\frac{X_5 X_8 - X_6 X_7}{X_8 - X_6} \right).$$

$$B_3 = 0.$$

$$A_1 = \frac{A_2}{X_1} \left[1 + \frac{X_2(X_5 - X_7)}{X_8 - X_6} \right] - \frac{F_1}{X_1}.$$

$$B_1 = -A_1 e^{2\pi\mu(z_c)^{2i\mu}} - \frac{g\hat{Q}}{c_p T_0 N_1^2} e^{\pi\mu i(z_c)^{-1/2+i\mu}}.$$

where

$$X_1 = 1 - e^{2\pi\mu(z_c)^{2i\mu}}(d - z_c)^{-2i\mu},$$

$$X_2 = (d - z_c)^{-2i\mu},$$

$$X_3 = 1 - e^{2\pi\mu(z_c)^{2i\mu}} \frac{1/2 - i\mu}{1/2 + i\mu} (d - z_c)^{-2i\mu},$$

$$X_4 = \frac{1/2 - i\mu}{1/2 + i\mu} (d - z_c)^{-2i\mu},$$

$$X_5 = (z_1 - z_c)^{1/2+i\mu},$$

$$X_6 = (z_1 - z_c)^{1/2-i\mu},$$

$$X_7 = \frac{1}{i\lambda} \left(-\frac{1}{2} + i\mu \right) (z_1 - z_c)^{-1/2+i\mu},$$

$$X_8 = \frac{1}{i\lambda} \left(-\frac{1}{2} - i\mu \right) (z_1 - z_c)^{-1/2-i\mu},$$

$$F_1 = \frac{g\hat{Q}}{c_p T_0 N_1^2} \left[(d - z_c)^{-1/2-i\mu} - i e^{\pi\mu(z_c)^{-1/2+i\mu}} (d - z_c)^{-2i\mu} \right],$$

$$F_2 = \frac{g\hat{Q}}{c_p T_0 N_1^2} \left[\frac{1/2 - i\mu}{1/2 + i\mu} e^{\pi\mu(z_c)^{-1/2+i\mu}} (d - z_c)^{-2i\mu} \right].$$

References

- Booker, J. R., Bretherton, R., 1967: The critical layer for internal gravity waves in a shear flow. *J. Fluid Mech.*, **27**, 513–539.
- Chun, H.-Y., 1991: Role of a critical level in a shear flow with diabatic forcing. Ph. D. dissertation, North Carolina State University, U.S.A., 159pp.
- Chun, H.-Y., Lin, Y.-L., 1995: Enhanced response of an atmospheric flow to a line-type heat sink in the presence of a critical level. *Meteorol. Atmos. Phys.*, **55**, 33–45.
- Fovell, R. G., Ogura, Y., 1988: Numerical simulation of a midlatitude squall line in two-dimensions. *J. Atmos. Sci.*, **45**, 3846–3879.
- Fovell, R. G., Ogura, Y., 1989: Effects of vertical wind shear on numerically simulated multicell storm structure. *J. Atmos. Sci.*, **46**, 3144–3176.
- Fovell, R. G., Dailey, P. S., 1995: The temporal behavior of numerically simulated multicell-type storms. Part I: Modes of behavior. *J. Atmos. Sci.*, **52**, 2073–2095.
- Houze, R. A., Jr., 1993: *Cloud Dynamics*. New York: Academic Press, 573pp.
- Klemp, J. B., Durran, D. R., 1983: An upper boundary condition permitting internal gravity wave radiation in numerical mesoscale models. *Mon. Wea. Rev.*, **111**, 430–444.
- Lin, Y.-L., Smith, R. B., 1986: Transient dynamics of airflow near a local heat source. *J. Atmos. Sci.*, **43**, 40–47.
- Lin, Y.-L., Chun, H.-Y., 1991: Effects of diabatic cooling in a shear flow with a critical level. *J. Atmos. Sci.*, **48**, 2476–2491.
- Lin, Y.-L., Wang, T.-A., Weglarz, R. P., 1993: Interactions between gravity waves and cold outflows in a stably stratified uniform flow. *J. Atmos. Sci.*, **50**, 3790–3816.
- Lin, Y.-L., Deal, R. L., Kulie, M. S., 1998: Mechanisms of cell regeneration, development, and propagation within a two-dimensional multicell storm. *J. Atmos. Sci.*, **55**, 1867–1886.
- Orlanski, I., 1976: A simple boundary condition for unbounded hyperbolic flows. *J. Comput. Phys.*, **21**, 251–269.
- Pandya, R. E., Durran, D. R., 1996: The influence of convectively generated thermal forcing on the mesoscale circulation around squall lines. *J. Atmos. Sci.*, **53**, 2924–2951.
- Rotunno, R., Klemp, J. B., Weisman, M. L., 1988: A theory for strong, long-lived squall lines. *J. Atmos. Sci.*, **45**, 463–485.
- Smith, R. B., Lin, Y.-L., 1982: The addition of heat to a stratified airstream with application to the dynamics of orographic rain. *Quart. J. Roy. Meteor. Soc.*, **108**, 353–378.
- Weisman, M. L., Klemp, J. B., 1982: The dependence of numerically simulated convective storms on vertical shear and buoyancy. *Mon. Wea. Rev.*, **110**, 504–529.
- Xue, M., Droegemeier, K. K., Wong, V., Shapiro, A., Brewster, K., 1995: *ARPS version 4.0 User's Guide*. Center for Analysis and Prediction of Storms, University of Oklahoma, 380pp.
- Yang, M.-J., Houze, R. A., Jr., 1995: Multicell squall-line structure as a manifestation of vertically trapped gravity waves. *Mon. Wea. Rev.*, **123**, 641–661.

Authors' addresses: Hye-Yeong Chun and In-Sun Song, Department of Atmospheric Sciences, Yonsei University, Seoul 120-749, Korea; Jong-Jin Baik, Department of Environmental Science and Engineering, Kwangju Institute of Science and Technology, Kwangju 506-712, Korea.